Nickel-based Single-Molecule Catalysts with Synergistic Geometric Transition and Magnetic Field-assisted Spin Selection Outperforms RuO_2 for Oxygen Evolution

Kavish Saini,[1] Aruna N Nair,[1] Anju Yadav,[1] Lissette Garcia Enriquez,[1] Christopher J. Pollock,[2] Stephen D. House, [3] Shize Yang,[4] Xin Guo,[4] and Sreeprasad T. Sreenivasan[1 *]

[1]Department of Chemistry and Biochemistry, The University of Texas at El Paso, El Paso, TX, 79968, USA

[2]Cornell High Energy Synchrotron Source, Wilson Laboratory, Cornell University, Ithaca, New York 14853, USA

[3]Center for Integrated Nanotechnologies, Sandia National Laboratories, Albuquerque, NM, 87111, USA

[4]Eyring Materials Center, Arizona State University, Tempe, Arizona, 85287, USA

*** Corresponding Author**: Sreeprasad T. Sreenivasan; Email: sreenivasan@utep.edu, Phone number; +1 (915) 747-6833, *https://orcid.org/0000-0002-5728-0512*

KEYWORDS **–** Single Molecule Catalyst, In-situ Geometrical Changes, Paramagnetic Ni Center, Magnetic Field, Spin-polarized OER

Abstract

Overcoming slow kinetics and high overpotential in electrocatalytic oxygen evolution reaction (OER) requires innovative catalysts and approaches that transcend the scaling relationship between binding energies for intermediates and catalyst surfaces. Inorganic complexes provide unique catalyst designs with customizable geometries, which can help enhance their efficiencies. However, they are unstable and susceptible to oxidation under extreme pH conditions. Immobilizing complexes on substrates creates single-molecule catalysts (SMCs) with functional similarities to single-atom catalysts (SACs). Here, an efficient SMC, composed of dichloro(1,3-bis(diphenylphosphino)propane) nickel [NiCl2dppp] anchored to a graphene acid (GA), is presented. This SMC surpasses ruthenium-based OER benchmarks, exhibiting an ultra-low onset and overpotential at 10 mAcm-2 when exposed to a static magnetic field. Comprehensive experimental and theoretical analyses imply that an interfacial charge transfer from the Ni center in NiCl2dppp to GA enhances the OER activity. Spectroscopic investigations reveal an in-situ geometrical transformation of the complex and the formation of a paramagnetic Ni center, which under a magnetic field, enables spin-selective electron transfer, resulting in enhanced OER performance. The results highlight the significance of in-situ geometric transformations in SMCs and underline the potential of an external magnetic field to enhance OER performance at a single-molecule level, pushing the boundaries of volcano limits.

1. Introduction

Electrochemical energy devices, such as water-splitting devices,[1] metal-air batteries,[2] and fuel cells[3–5] have limited practical use due to their dependence on precious metal catalysts for enhancing the kinetics of oxygen electrocatalytic reactions like oxygen evolution reaction (OER) and oxygen reduction reaction (ORR). Using expensive and scarce catalysts makes energy from these devices costly and commercially unviable. As a result, researchers propose both homogeneous and heterogeneous alternative catalysts to replace these precious metal benchmarks.[1,2] Homogenous catalysts, evenly distributed in a reaction mixture, provide the highest catalyst efficiency and activity. However, heterogeneous catalysts are preferred for industrial applications due to their ease of use and increased stability under harsh conditions. Though a few metal-free heterogeneous catalysts have been reported, bimetallic catalysts and catalysts based on sustainable and abundant materials, such as earth-abundant metals, still exhibit significantly higher catalytic activity.[3] Among heterogeneous catalysts, single-atom catalysts (SACs) have emerged as promising candidates due to their high atom efficiency and lower metal content. While significant progress has been made in developing SACs with high OER efficiency and mass activity,[4–8] the challenge of enhancing their surface density and preventing the aggregation of active sites during operation into clusters that reduce their activity remains a bottleneck.

Coordination complexes, formed by the interaction of a metal ion with ligands, display a wide array of structural and chemical properties that depend on the metal ion, ligand type, and coordination geometry.[9] Such design flexibility enables their use in various fields, including catalysis[10], magnetic materials[11], and biological systems.[12] In particular, coordination complexes are widely explored as homogeneous catalysts, as their unique structural topologies facilitate the formation of well-defined catalytic sites. The coordination of individual metal ions with ligands generates highly active "single-atom coordinated molecular sites," resulting in high catalytic efficiency.[13–16] Moreover, modifying the metal ion, ligand, or coordination environment can tune the structural and chemical properties of complexes, [17–19] enabling the development of catalysts with specific activities for a wide range of reactions, including oxygen electrocatalysis.[20]-[21] For example, nickel selenide ($[Ni\{(SeP^{i}Pr_2)_2N\}_2]$)[22] and $[M(OTf)_2(Me_2Pytacn)]$ (M = Ni, Co, Fe, Mn, OTf = $CF_3SO_3^{2-}$)[10] complexes are reported to catalyze OER effectively. However, coordination complex-based catalysts have some limitations that restrict their utility.[23] In addition to the difficulty of separating or recovering them from the reaction mixture, one of the major challenges is their instability.[24] In some cases, the organic ligands in the coordination complex can undergo oxidation and form metal oxides that can negatively impact the catalytic activity of the complex.[25,26] Additionally, many coordination complexes are sensitive to environmental conditions, such as pH and temperature, and can undergo ligand exchange or degradation, leading to the loss of catalytic activity or the formation of unwanted side products.[27,28]

Various strategies are practiced to enhance the stability and performance of coordination complexes-based catalysts, such as using protective ligands and nanostructured substrates to anchor the complexes.[29] The latter case involves extending the SAC concept to coordination complexes and immobilizing on suitable supports. Anchoring organometallic complexes to conducting supports, such as graphene oxide or acetylene black, can enhance their stability while maintaining or boosting their catalytic activity.[30–34] For instance, heterogenization of cobalt complexes by immobilizing them on doped graphene improved electronic communication and enhanced CO_2 reduction.[35] In contrast to Co-complexes, nickel-based coordination complexes[22] have shown great promise as potential OER catalysts due to their low overpotentials, good stability, and high reaction rates.[36–40] Despite their extensive study as homogeneous catalysts,[41–43] the use of nickel-based coordination complexes as heterogeneous catalysts is poorly investigated.[44] We contend that immobilizing OER active Ni complexes on conductive supports could improve their stability and catalytic performance towards OER.

In addition to designing novel catalysts, researchers have applied various innovative strategies, including improving mass transfer,[45] increasing the intrinsic activity and number of active sites,[46],[47] modulating electronic structure,[47–49] and increasing the exposed surface area,[50–52] to significantly reduce OER overpotentials. Nonetheless, many catalysts still show several hundreds of mV overpotential for OER. One of the reasons for this high overpotential is the spin state transition that is necessary between the reactants and products during OER. The OER is a quantum-mechanically prohibited process involving the conversion of diamagnetic oxygen species (such as OH or water) to paramagnetic oxygen molecules. This means additional energy is required to drive the reaction, resulting in high overpotentials.[53,54] Recently, the spin polarization in magnetic catalysts under a magnetic field has been shown to significantly decrease the barrier for transferring an electron with a selective spin (spin filtering) and increase the efficiency of OER.[55] Although the benefits of applying a magnetic field on catalytic processes are well-established, until recently, the impact on electrocatalysis was attributed to various indirect effects,[56–58] while spin-based effects were largely overlooked. However, after Garcia's[53,54] prediction about the spin-dependence of electrocatalytic water splitting, significant research has explored magnetic catalyst-induced spin effect experimentally. Most spin-based enhancement has been reported in ferromagnetic bulk catalysts,[59,60] with only a few examples of atomic or molecular systems.[61,62] Coordination complexes are ideal for studying the spin effects in molecular catalysts because they possess a well-defined crystal field, and the orbital occupancy and binding energy can be tuned by selecting the ideal ligands and crystal structure. Therefore, creating stable, heterogeneous coordination complex-based catalysts by immobilizing them on suitable substrates and enhancing their activity through spin regulation by an external magnetic field can open up new opportunities in oxygen electrocatalysis. However, to the best of our knowledge, such an effort has not yet been undertaken.

In this study, we developed a novel heterogeneous catalyst by immobilizing a Ni-based coordination complex on a graphene matrix through noncovalent interactions that spontaneously get magnetically active in an alkaline medium. We refer to this type of catalyst as single molecule catalysts (SMCs) due to their similarity to SACs in terms of their behavior as single molecules. The SMCs outperform typical SACs in both adaptability and versatility when it comes to fine-tuning their catalytic properties. Contrary to SACs, which primarily depend on metal-atom substrate interactions for activity tuning, SMCs provide the added flexibility of catalytic activity modification, not only through substrate interactions but also via customized coordination environments. This tailoring of the coordination environment can be achieved by altering the ligand structures, changing the number of coordinating ligands, or even substituting ligands with different molecules that possess similar base chemistry. Moreover, SMCs allow for the interchangeability of the metal center, by using different metals or different oxidation states of the same metal with the same set of ligands. This level of control at the molecular level enables precise tuning of catalytic properties in SMCs, rendering them superior to SACs. Our SMC incorporates a dichloro(1,3-bis(diphenylphosphino)propane) nickel, termed $NiCl_2$dppp hereafter, as the OER molecular catalyst due to the abundance of nickel and pnictogens, and its appropriate alignment of the conduction and valence band edges with the water oxidation potential.[63,64] We identified graphene acid (GA) as the ideal substrate to anchor the $NiCl_2$dppp complex due to its high conductivity, surface area, potential for interfacial charge transfer, and known stability under OER conditions.[65–67] The formulation of $NiCl_2$dppp complex anchored on GA (NiGA) catalysts enhances the stability and activity of the complex. Our results show that under OER conditions, the $NiCl_2$dppp complex undergoes a transition from square planar to trigonal bipyramidal geometry by coordinating with additional -OH ligands in the medium, resulting in a paramagnetic Ni^{2+} site. Leveraging the in situ generated paramagnetic centers in the catalysts, we present the first evidence that magnetically active single-molecule catalysts can significantly improve OER activity when exposed to a magnetic field. Through various experimental and theoretical investigations, we prove the in situ structural changes in the $NiCl_2$dppp complex that make it sensitive to external magnetic fields, leading to spin polarization and spin-selective catalysis that significantly reduce their onset potential (230 mV) as well as overpotential at 10 $mAcm^{-2}$ (η_{10} of 340 mV), substantially lower than benchmark Ru and Ir-based systems. We anticipate that the insights derived from the study will pave the way for magnetically active SMCs with peerless catalytic activity and contribute to future energy sustainability.

2. Results and Discussion

Analysis of structure and composition. Figure 1a depicts the preparation of $NiCl_2$dppp and NiGA SMC. Due to the presence of sp^2 hybridized carbons (π electrons) and other electron-rich atoms in the structure, we envisage different noncovalent interactions between the $NiCl_2$dppp complex and GA sheets, resulting in

the formation of the NiGA SMC. We analyzed the potential noncovalent interactions using Gaussian 16 (based on Reduced Density Gradient). Our analysis showed the possibility of hydrogen bonding between the lone pairs of chlorine atoms ($NiCl_2$dppp complex) and the hydrogen atoms of -OH groups on GA. Other interactions are predominantly van der Waals forces, including pi-pi stacking between the benzene rings of $NiCl_2$dppp complex and GA, and weak London dispersion forces. Steric effects from two phosphorous atoms and phenyl rings on the dppp can also be seen. Results of the analysis are shown in Figures 1b and 1c, with blue, green, and red regions representing H-bonding, van der Waals, and steric forces, respectively. The NiGA and $NiCl_2$dppp catalysts were examined using different spectroscopic techniques to better understand their structural and chemical properties. In our experiment, we prepared NiGA by combining $NiCl_2$dppp and GA at various weight ratios, including 1:1 (5mg:5mg), 2:1 (10mg:5mg), 3:1 (15mg:5mg), and 4:1 (20mg:5mg). The best catalytic activity was demonstrated by the 2: 1 NiGA sample (data shown later in the electrochemical characterization section) and hence was analyzed in detail. First, the successful formation of the $NiCl_2$dppp complex was confirmed using ^{1}H and ^{31}P Nuclear Magnetic Resonance (NMR) spectroscopy (Figure S1a and S1b). To obtain more detailed structural information, we crystallized the $NiCl_2$dppp and analyzed it using single-crystal X-ray diffraction (SC-XRD) (Figure S2 and Table S2). The SC-XRD confirmed that the $NiCl_2$dppp complex has a square planar geometry. The samples were also analyzed using powder X-ray diffraction (PXRD). Figure 1d illustrates the PXRD profiles for GA, $NiCl_2$dppp, and NiGA SMCs. The P-XRD profiles of the $NiCl_2$dppp complex and NiGA had close similarity indicating the successful anchoring of the complex on GA and that the complex retains its structure in the NiGA SMC. Detailed analysis showed that, compared to $NiCl_2$dppp, features around 25º (2θ) were slightly broader, and the background intensity increased. The above change may be due to the graphitic (002) feature seen at 24.9º in GA merging with the $NiCl_2$dppp features in NiGA. We simulated and compared the XRD spectrum to the experimental spectrum to confirm this observation. Figure 1e shows the experimental (observed) and simulated (calculated) PXRD patterns of NiGA. With a 96% match and minimal differences, it is clear that the proposed structure is accurate for the prepared NiGA SMC. To gain a deeper understanding of the chemical nature and to identify any potential charge transfer of metal sites, we analyzed the samples using X-ray photoelectron spectroscopy (XPS). Figures 1f-k, S3, and S4 show the XPS analysis of NiGA and its components. While GA did not exhibit any presence of Ni (Figure S3b), $NiCl_2$dppp and NiGA demonstrated Ni features, confirming the presence of Ni center due to $NiCl_2$dppp. Figures 1g and h show the high-resolution XPS spectrum of the Ni 2p region of $NiCl_2$dppp and NiGA, confirming that Ni is present in the Ni^{2+} state in both structures. Interestingly, we observed a shift of ~80 meV for Ni in the NiGA complex compared to the $NiCl_2$dppp complex, which could be attributed to charge transfer between GA and $NiCl_2$dppp in NiGA.[68] We also analyzed the high-resolution carbon 1s spectra for NiGA, GA, and $NiCl_2$dppp, respectively (Figure i-k). Further, the C1s spectrum of NiGA upon deconvolution (Fig. 1i)

demonstrated four components, comprising the prominent sp^2 carbon feature from the $NiCl_2$dppp complex and GA and the other features corresponding to the functional groups in GA.[69] We tested the thermal stability of $NiCl_2$dppp complex and NiGA and confirmed that the $NiCl_2$dppp and NiGA are stable up to 60 ºC (Figure S5).

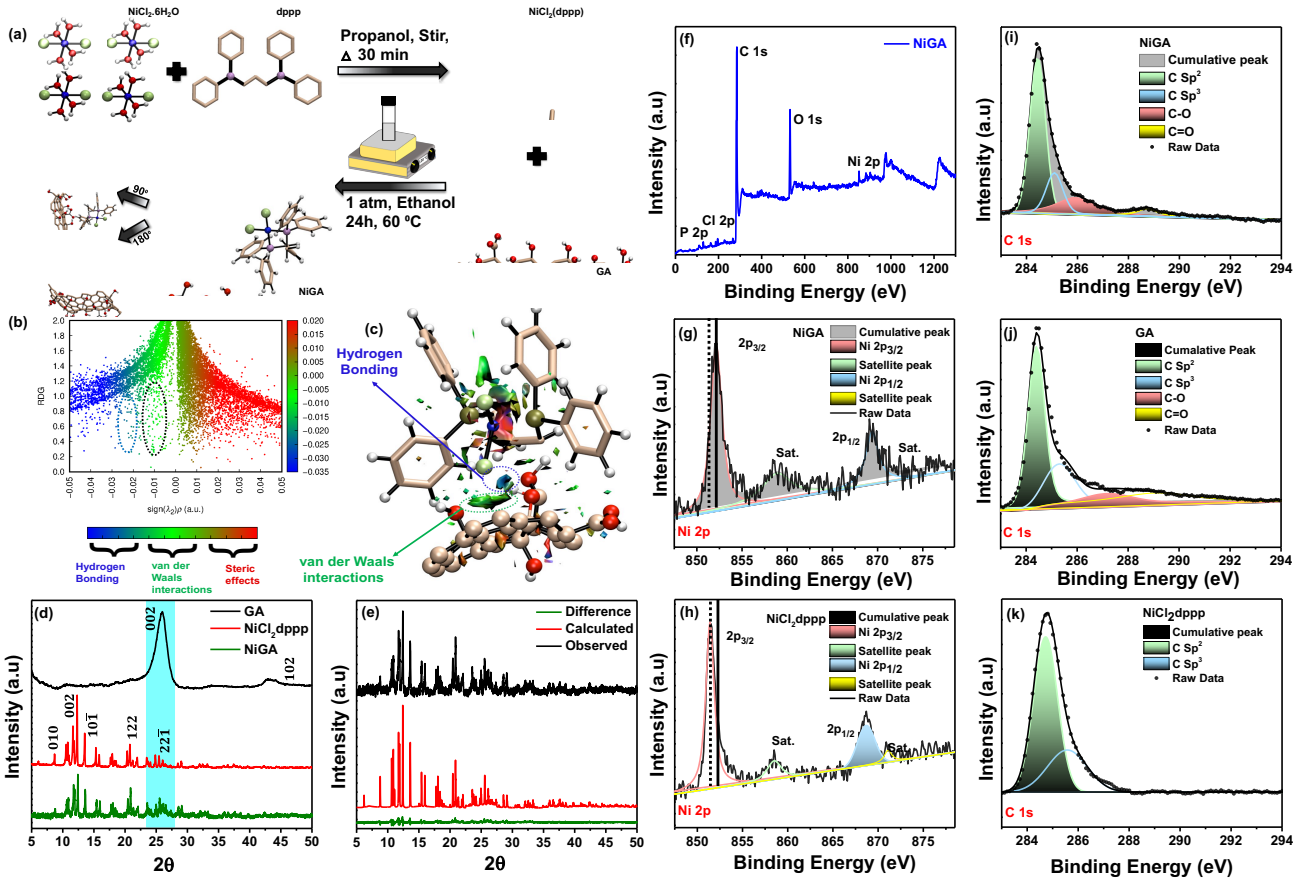

Figure 1 (a) Schematic depicting the preparation process of $NiCl_2$dppp and NiGA SMCs (atoms selection by color: Blue, green, purple, nude, red, and white correspond to nickel, chlorine, phosphorus, carbon, oxygen, and hydrogen, respectively) (b) shows the scatter plot of the Reduced Density Gradient (RDG) function plotted w.r.t the electron density, $\boldsymbol{\rho}$. (c) shows the RDG isosurface for the fragment, including $NiCl_2$dppp and Graphene Acid (GA). (d) PXRD profiles of as-synthesized GA, $NiCl_2$dppp & NiGA (e) Comparison of observed PXRD pattern of NiGA with simulation calculation (f) Survey XPS for NiGA (g-h) Ni 2p XPS spectrum of NiGA and $NiCl_2$dppp (i-k) C 1s XPS spectrum of NiGA, GA, and $NiCl_2$dppp.

Microscopic morphology analysis. After confirming the structure and chemical configuration of NiGA, we investigated the morphology of NiGA SMC using different microscopic techniques. High-resolution high-angle annular dark-field scanning transmission electron microscopy (HAADF-STEM) analysis of the NiGA catalyst confirmed the presence of the $NiCl_2$dppp complex anchored on the GA sheet, as shown in Figure

2a. The HAADF-STEM image displayed clear white bright spots <0.1 nm in size – corresponding to the individual Ni atoms – in addition to the wrinkled multilayer sheets and edges in GA, indicating the potential molecular nature of the supported $NiCl_2$dppp complex in NiGA. Compared to the high-resolution transmission electron microscopy (HRTEM) image (Figure 2b), HAADF-STEM better identified the presence of $NiCl_2$dppp in the NiGA SMC. Electron energy loss spectroscopy (EELS) spectra (Figure 2c) were collected from an equivalent region as the STEM image (Figure S6), revealing the signal of Ni (L-edge), C (K-edge), and P (L-edge). The samples were also examined using atomic force microscopy (AFM). Considering the lower resolution of AFM to identify molecules and get a better image, we used a higher concentration of $NiCl_2$dppp in the NiGA sample (4:1) used for AFM analysis. The AFM analysis showed a preferential binding of $NiCl_2$dppp on the GA sheet, presumably due to different noncovalent interactions (as indicated in Figures 1 b and c). The AFM image and the height profiles for NiGA in Figure 2d show that the GA substrate comprises multiple sheets (thicknesses of ~12nm) and some large assembled structures of $NiCl_2$dppp (thicknesses of ~200 nm), respectively. Assembly of similar complexes at high concentrations to form bigger aggregates is reported.[70] This was further confirmed by the AFM analysis of the $NiCl_2$dppp complex alone, which showed similar aggregated structures (Figure S7). Further, aggregates were also observed in HRTEM analysis of samples with a higher content of $NiCl_2$dppp (Figure S6) in NiGA (4:1). Our scanning electron microscopy (SEM) analysis of the NiGA sample (Figure 2e) further confirms the sheet-like morphology of the NiGA SMC, while energy dispersive spectroscopy (EDS) analysis and elemental maps in Figure 2e confirms the presence of uniformly distributed Ni on the GA sheets. The corresponding EDS spectrum is given in Figure S8.

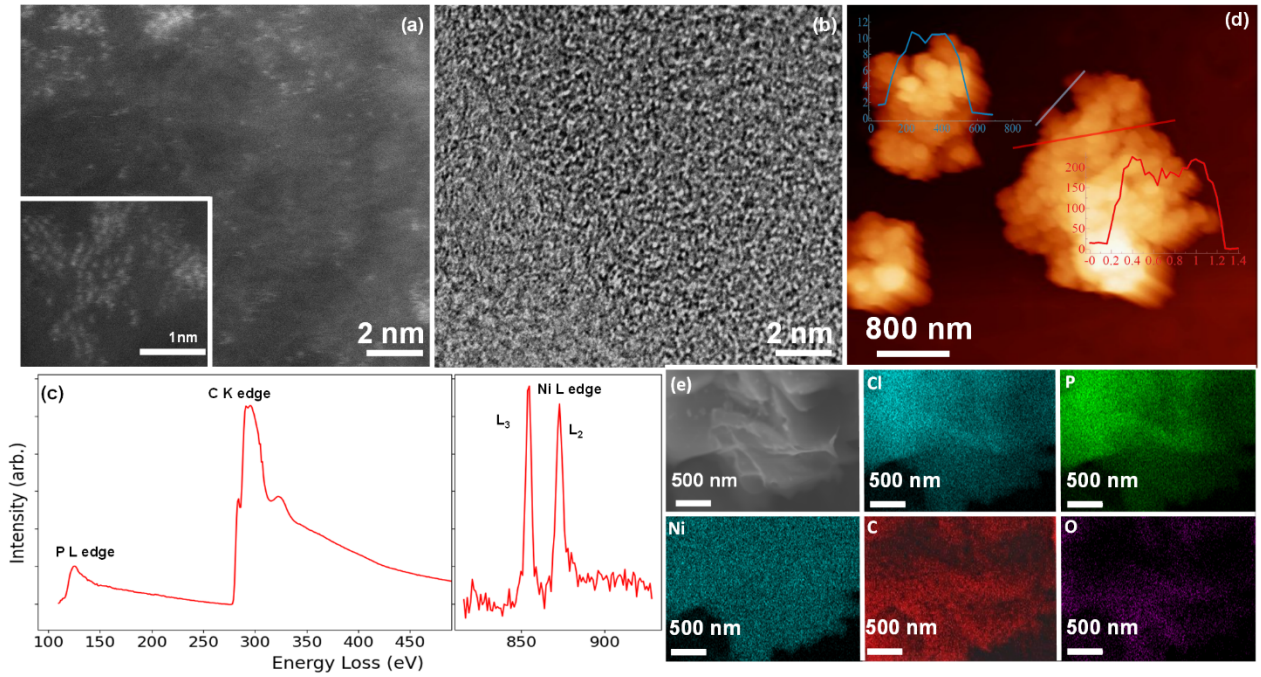

Figure 2 (a) High-angle annular dark-field scanning transmission electron microscopy (HAADF-STEM) image and (b) HRTEM images of NiGA (c) EELS spectrum from an equivalent region shown in HAADF-STEM image for NiGA. (d) AFM image of NiGA and height profiles from two different regions showing the thickness of multilayer GA sheets and the aggregates of $NiCl_2$dppp. (e) SEM image of NiGA sample and the corresponding elemental maps.

Spectroscopic investigation of in-situ geometry change. Our initial SC-XRD and XPS analysis confirmed that the $NiCl_2$dppp complex is square planar with a Ni^{2+} metal center. However, under extreme pH conditions encountered during electrocatalysis, coordination complexes can undergo structural changes by modifying their coordination environment.[24–27] For example, $^{-}$OH ions, which are abundant under alkaline OER conditions, can function as a ligand, replace labile ligands (such as Cl^-), and increase coordination. The thermodynamic energy analysis of the possible coordination changes is given in Figure S9 and table S3. For $NiCl_2$dppp, besides replacing Cl-, adding extra -OH to the Ni center can result in three potential structures: square pyramidal or trigonal bipyramidal (TBP) with one additional OH attachment (coordination number 5) and octahedral when two OH groups (coordination number 6) attached. However, the formation of an octahedral complex is unlikely due to the unfavorable bite angle of dppp, which is the angle between two phosphorus atoms and the metal center.[71] Here, adding two extra -OH ligands in our Ni complex would lead to a bite angle of approximately 82°, which is insufficient to stabilize an octahedral structure.[72] Moreover, in an octahedral complex, hydrogen atoms on the carbon chain can interact with other OH (or Cl, if not replaced) ligands, causing ligand dissociation and reverting to a square planar complex.[73] This further decreases the chances of forming an octahedral complex. Among the two possible geometries for five coordinated complexes, trigonal bipyramidal (TBP) and square pyramidal, TBP is expected to be the most feasible structure. In square pyramidal geometry, the incoming hydroxyl ion ($^{-}$OH) would face resistance due to the out-of-plane carbon chain connected to two phosphorus atoms, making it a less favorable configuration compared to TBP.[74] We used Addison's model to verify that the TBP geometry is the most feasible intermediate configuration.[75] According to this model, $\boldsymbol{\tau}_5$ represents the "index of the degree of trigonality" and is calculated from the two largest bond angles in the structure (labeled as α and β, see Figure S10). A $\boldsymbol{\tau}_5$ of 0 indicates square pyramidal geometry, while a $\boldsymbol{\tau}_5$ of 1 indicates trigonal pyramidal geometry.[76] Our calculated $\boldsymbol{\tau}_5$ is 0.956, which is close to 1, indicating that the complex may prefer to form a distorted trigonal bipyramidal structure. The equatorial Jahn-Teller distortion for TBP geometry is necessary to remove the degeneracy by splitting the d orbitals.[77] However, dimerization can occur in the case of Ni complexes in presence of multiple OH ligands, leading to the formation of square planar dimers.[78] Thus, during electrocatalysis, it is possible that an additional hydroxyl ion (OH-) may coordinate with the Ni^{2+} center, forming an equatorially distorted TBP or a square pyramidal complex as a dimer.

To experimentally investigate the potential changes in coordination environment and geometry, we analyzed the $NiCl_2$dppp complex with and without KOH using UV/Vis absorption spectroscopy. The optical spectra were obtained in dichloromethane (DCM) and are provided in the Figure S11. The $NiCl_2$dppp complex has a square planar geometry with C_{2v} symmetry and can exhibit four possible spin-allowed d-d transitions. Among these transitions, the transition from $^1A_1$ to $^1B_2$ occurs at approximately 600 nm, while the other three transitions ($^1A_1$ to $^1A_2$, $^1A_1$ to $^1A_2$, and $^1A_1$ to $^1B_1$) overlap with the charge transfer bands in the higher energy region.[79] The spectrum of the pristine $NiCl_2$dppp complex in DCM showed a broad feature at around 600 nm, confirming the square planar geometry. However, this feature disappears when the complex is exposed to KOH (in DCM + methanol + KOH), indicating a change in coordination environment. Note that the feature at 300nm seen in Figure S11 is due to methanol present in the system. The transition of Ni centers from square planar to higher coordination number geometries can generate unpaired electrons, resulting in magnetic properties (paramagnetism) for the Ni complex.[80] Consequently, we investigated the potential magnetism in the in-situ generated Ni species using electron paramagnetic resonance (EPR) spectroscopy. For this, we simulated the electrochemical cell environment in the EPR tube using methanol and KOH. However, to minimize the effects of dipole moments from polar molecules and their interference with the EPR microwave, we utilized a custom-made aqueous cell for the measurement, as shown in the inset of Figure 3a.[81] Our continuous wave (CW) EPR demonstrated a distinct magnetic resonance signal due to the presence of unpaired electrons (Figure 3a). The results are consistent with other reported paramagnetic complexes containing Ni^{2+} centers, [82–84] indicating that the in-situ generated Ni complex is indeed paramagnetic. To further verify the in-situ change in coordination environment suggested by UV/Vis and EPR spectroscopy, and to estimate the potential number of unpaired electrons in the resulting complex, we analyzed the in-situ transformation using nuclear magnetic resonance (NMR) spectroscopy. This is feasible because the change in coordination and geometry also leads to a modification in the magnetic properties of the $NiCl_2$dppp complex. The initial $NiCl_2$dppp complex is square planar, diamagnetic, and lacks unpaired electrons. However, as previously postulated, upon changing the coordination number to 5 and the geometry to TBP (or square pyramidal), the d-orbital splitting will change, resulting in the generation of unpaired electrons and the complex will exhibit paramagnetism. This change from a diamagnetic to paramagnetic species can be examined using NMR spectroscopy through the Evans method, which evaluates magnetic susceptibility based on the paramagnetic chemical shift based on a reference chemical shift in a solvent.[85] For this, we simulated the environment of our electrochemical cell and applied them to the complex in an NMR tube. Figure 3b displays the results of the ^1H NMR-based experiment following the Evans method.[85] The inset in Figure 3b shows the coaxial NMR tube, containing an inner and outer tube filled with a reference solvent (methanol + methanol-d_4) and the complex in a solvent system that simulates the electrocatalytic reaction environment (methanol + methanol-d_4 + $NiCl_2$dppp SMC +KOH), respectively. The relative

frequency shift ($\Delta\nu = \nu_{\text{methanol}} - \nu_{\text{methanol+ NiCl2dppp}}$) is 56Hz, and the magnetic susceptibility and moment calculations are 0.00323 cm^3/mol and 2.74 μB, respectively (see calculations in supporting information 11 and composition in table S4). The magnetic moment value suggests the presence of two unpaired electrons in the solution, indicating that the complex is paramagnetic in the electrochemical environment, potentially due to the conversion to TBP (or square pyramidal) geometry. As the OH ligand has moderate strength, the complex will have a high spin configuration, regardless of whether it adopts TBP or square pyramidal geometry, both having two unpaired electrons (see Figure S12). Therefore, determining whether the complex is TBP or square pyramidal is not possible in this case, using the Evans method. However, our experiments proved the spontaneous, in-situ change of square planar, diamagnetic $NiCl_2$dppp in the presence of KOH to a paramagnetic species with potentially 2 unpaired electrons (TBP or square pyramidal). Figure 3c illustrates the scheme of the geometry change for $NiCl_2$dppp to TBP complex.[77]

To further confirm the single molecule nature of the catalysts and to probe porposed geometrical changes in NiGA, we analyzed the samples using X-ray absorption near edge spectra (XANES) and extended x-ray absorption fine structure (EXAFS) methods. The XANES data for parent $NiCl_2$dppp, NiGA (after treatment with KOH), and Ni metal foil are shown in Figure 3d. Both $NiCl_2$dppp, and NiGA display XANES spectra shifted to higher energy relative to Ni metal and possess clearly defined pre-edges, both features indicative of Ni in an oxidized, non-metallic state (Ni^{2+} as verified by XPS). The shape of $NiCl_2$dppp, is consistent with Ni coordinated to P and Cl ligands while NiGA shows a more intense white line and higher energy rising edge, consistent with partial or complete substitution of Cl ligation with lighter atoms (e.g. O, N), [85] potentially due to the ligand subsitition or attaching incoming OH^- ligand when NiGA is treated with KOH. The nearly identical pre-edge energies of $NiCl_2$dppp and NiGA indicate similar metal oxidation states for both species, suggesting that the geometric and/or ligand changes do not result in a change in the metal oxidation state. To support and augment the conclusions drawn from the XANES, the EXAFS for $NiCl_2$dppp and NiGA were fit to determine nearby scattering partners and distances (Figure 3e-h) and EXAFS data for Ni-foil is shown in Figure S13. The fit for $NiCl_2$dppp contains 4 P / Cl scatterers at 2.21 A, as expected based on the above characterization. For NiGA, poor fits were obtained when attempting to fit the data using a single shell of either P / Cl or O / N scatterers (Table S5 and S6), though excellent agreement with experiment was found by including one shell of two O / N scatterers at 1.99 A and another shell of two P / Cl scatterers at 2.21 A. This result confirms the qualitative XANES assessment of partial replacement of the initial ligand sphere with OH ligands. Also notably, neither $NiCl_2$dppp nor NiGA display any long-range scattering that would suggest the presence of Ni-Ni interactions. Taking the XANES and EXAFS results together, these x-ray data provide strong evidence against metal cluster formation and confirms that the Ni complexes remain isolated within the NiGA structure (with partial ligand exchange with OH), further confirming that the NiGA is single molecule catalyst. While the best EXAFS fit for NiGA exposed to KOH had an overall coordination

number of four (two O and two P scatterers), due to the limitations of EXAFS analysis this fit should be viewed as entirely consistent with the NMR and EPR findings of a 5-coordinate Ni center. Namely, beyond the inherent +/-25% uncertainty of the coordination number parameter in EXAFS fits, in cases where multiple shells of scatterers are in close proximity-as is the case here coordination number findings are known to be artificially depressed due to the failure of the Debye-Waller factor to properly account for the non-Gaussian spatial distribution in such systems.[86] As such, it is reasonable to conclude that the actual Ni coordination number could be somewhat higher from that determined from the fits. Indeed, Table S6 reveals that overall 5-coordinate fits (2 P/Cl + 3 O/N) also yield excellent agreement with the experimental data.

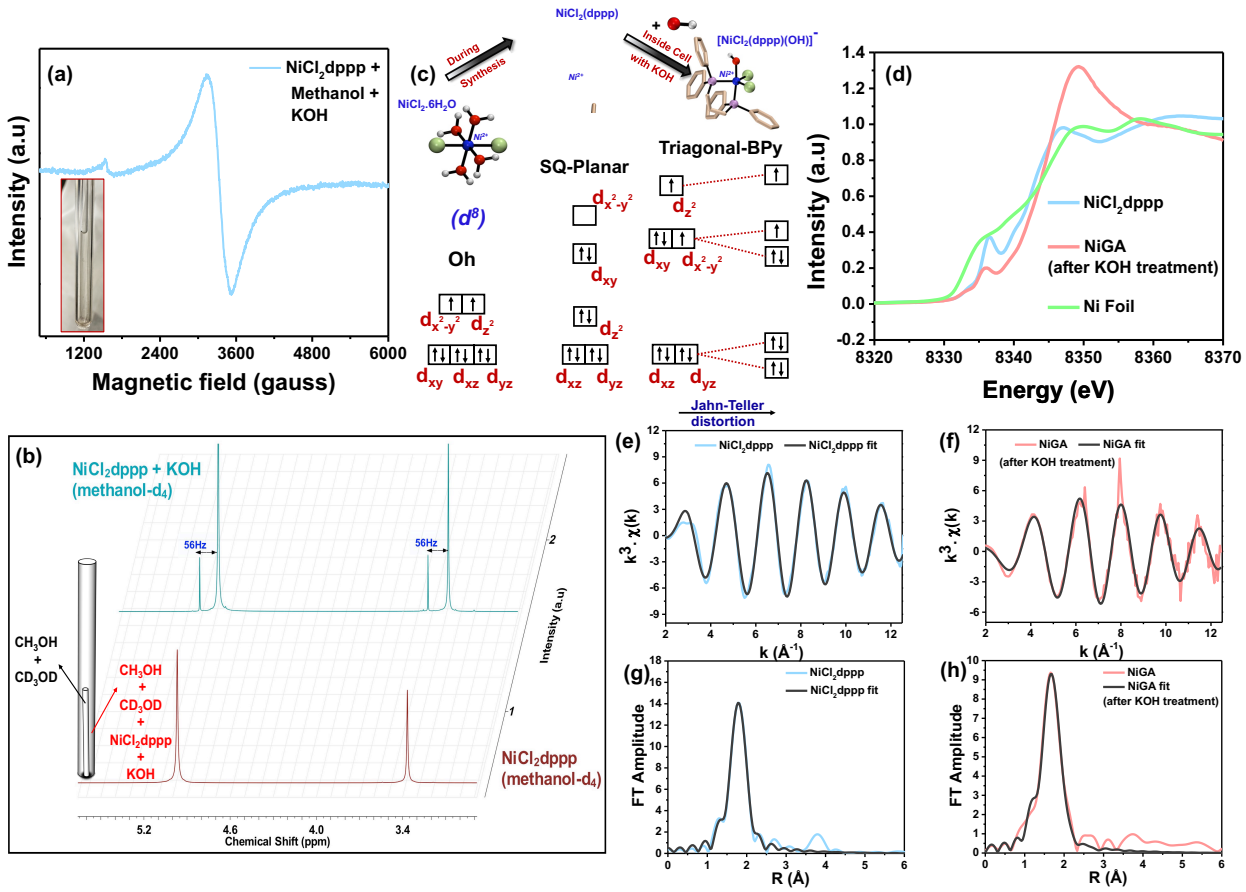

Figure 3 (a) continuous wave electron paramagnetic resonance (CW-EPR) and (b) ^{1}H NMR Evans method showing the paramagnetic nature of $NiCl_2$dppp under alkaline conditions, illustrating the geometrical change, and (c) Schematic showing possible structural conversion and change in the electronic configuration of nickel center. (d) Comparisons of XANES spectra of $NiCl_2$dppp, NiGA after treating with KOH, and Ni foil (e-f) EXAFS spectrum in k-space (k^3-weighted) derived from normalized absorption for $NiCl_2$dppp and NiGA (g-h) Fourier transformed (FT) EXAFS spectrum (R-space) indicating a lack of Ni-Ni interactions in catalysts.

Electrochemical Oxygen Evolution Reaction (OER). After confirming the formation and structure of the catalysts, we analyzed the electrochemical OER activity of the prepared catalysts, NiGA and its components. Figure 4a shows the current densities (j) normalized by the geometric area of the electrode (0.071 cm^2) for the different samples. Notably, both $NiCl_2$dppp and NiGA (2:1) exhibit a sharp increase in current density corresponding to the evolution of O_2, indicating a facile OER process. The linear sweep voltammetry (LSV) revealed a notable feature within the 1.40 to 1.45 V range, attributed to the $Ni^{2+/3+}$ redox couple. This observation verifies the electrochemical accessibility of Ni atoms in the in situ generated Ni complex and the true OER catalytic center is Ni^{3+}, as reported previously.[22,44,87,88] Notably, the Ni complex is anticipated to maintain stability, due to the known enhanced stability of Ni complexes bound to low electronegativity pnictogens atoms. [89] Consequently, the presence of two Ni^{3+}-P bonds in the catalyst is expected to ensure its stability under OER conditions, where the initiation of the OER starts by the coordination of OH^- on the metal without affecting the Ni-P bonds. The onset potential for $NiCl_2$dppp, NiGA, RuO_2, and GA were 1.55 V, 1.49 V, 1.48 V, and 1.57 V versus RHE, respectively. Compared to the components, NiGA SMC shows remarkable OER performance with an overpotential η_{10} of 400 mV, which is comparable to the benchmark RuO_2 (390 mV). The OER activity was also confirmed by analysis using calomel electrode which did not show any change in the onset or overpotentials (Figure S15). Figure S16 confirms that an increase or decrease in $NiCl_2$dppp in the SMC leads to decreased activity, thus validating the 2:1 NiGA as the ideal catalyst composition. A lower amount of $NiCl_2$dppp reduces the number of potential active sites, whereas a higher concentration can cause the formation of multilayer aggregates (as shown in the microscopic investigations in Figure S6 and S7), reducing the number of accessible active centers. To understand the catalytic mechanism and kinetics of the OER, we conducted a Tafel plot analysis (Figure 4b). Our analysis revealed Tafel slopes of 59.1, 85.3, 54.5, and 134.2 $mVdec^{-1}$ for NiGA, $NiCl_2$dppp, RuO_2, and GA, respectively. It should be noted that NiGA has a smaller Tafel slope than $NiCl_2$dppp, indicating its better reaction kinetics. The Tafel slope of NiGA (59.1 $mVdec^{-1}$) is also comparable to RuO_2 (54.5 $mVdec^{-1}$), pointing to a similar OER mechanism with second step (O* formation) as the rate determining step (RDS), similar to other square planar nickel-macrocycle-based OER catalysts.[41] The performance parameters of various catalysts, such as onset potential, Tafel slopes, and mass activity, are compared in Table S7, highlighting the superior performance of NiGA. To better understand the reasons behind NiGA's improved electrochemical activity, we examined its charge transfer resistance (R_{ct}). The R_{ct} was determined through electrochemical impedance spectroscopy (EIS) measurements, as shown in Figure 4c. Clearly, NiGA shows a significantly reduced R_{ct} of ~160Ω compared to $NiCl_2$dppp (~510Ω), suggesting enhanced charge transfer kinetics in NiGA, potentially due to the presence of conductive GA in the sample.

We constructed a Molecular Electrostatic Potential (MEP) map for the $NiCl_2$dppp showing the electrostatic interaction energy to gather a preliminary understanding of the potential active sites. From the MEP of the complex, we can observe that the nickel center has a partial positive charge (indicated by the blue color) as it has a positive value of interaction energy. On the other hand, the chlorine atoms possess negative charge density (indicated by the red color) and have a negative interaction energy value. Therefore, Ni is the electron-deficient center (as indicated by the dotted black circle in Figure 4d) and the potential OER center in the complex. Subsequently, to understand the reason behind the improved catalytic activity of Ni center in NiGA compared to $NiCl_2$dppp, we conducted experimental and density functional theory (DFT)-based theoretical exploration of the catalysts. The formation of heterojunctions between two distinct components, as in the case of NiGA, is known to modify and control electronic properties, such as the band structure of materials.[90,91] Hence, we electrochemically estimated the HOMO-LUMO (or conduction and valence bands) levels of individual components (GA, $NiCl_2$dppp) and NiGA SMC (Figure S17). The formation of the NiGA SMC resulted in a decrease in its band gap compared to $NiCl_2$dppp and GA (Figure 4e), which could contribute to the lower charge-transfer resistance observed in the EIS measurement.[69] Furthermore, the valence band of NiGA was found to be closer to the OER standard potential (1.23V) compared to $NiCl_2$dppp or GA, probably contributing to improved OER activity. The relative band positions in $NiCl_2$dppp and GA indicate a potential electron transfer from the higher-lying $NiCl_2$dppp to the lower-lying GA, resulting in the development of a built-in potential. This electron transfer would make the Ni more positive and active for OER. Our XPS investigation (Figure 1g) clearly showed a shift to higher binding energy for the Ni 2p features in NiGA compared to $NiCl_2$dppp, confirming the proposed electron transfer. To better understand the observed OER activity in NiGA, we carried out DFT calculations to examine the energetics of the process. For this, we optimized the structure of the NiGA SMC with TBP geometry for $NiCl_2$dppp. Initially, we computed the free energy of the OER intermediates over NiGA and confirmed that among the various potential active sites investigated, Ni was the most favorable active site for OH adsorption based on the energy profile (see Figure S18). Our DFT calculations suggested that the second step of the OER process is the rate-determining step (RDS) for NiGA. Moreover, the Gibbs free energy profile for each individual OER step revealed that the energy required to transfer *OH to *O is lower for NiGA SMC (~0.70 eV) compared to $NiCl_2$dppp and GA. Interestingly, the difference in free energy (~1.9 eV) for NiGA is comparable to the benchmark RuO_2 (~1.5 eV), as shown in Figure 4f. All Gibbs free energy calculations and parameters can be found in Table S8 and S9. The density of states (DOS) profile of both $NiCl_2$dppp and NiGA shows that the combination of GA and $NiCl_2$dppp to form NiGA increases the electron density near the standard water splitting potential (1.23 V) (Figure 4g), which can also contribute to the improved OER performance of NiGA.

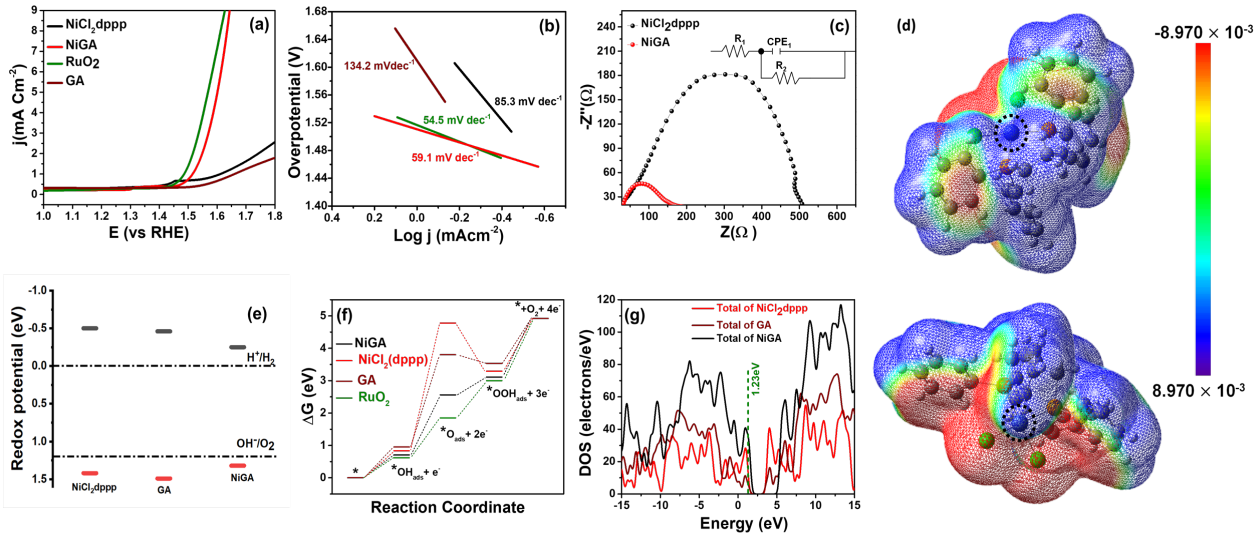

Figure 4 (a) Linear sweep voltammetry (LSV) of the $NiCl_2$dppp, NiGA, RuO_2 & GA for OER (b) Corresponding Tafel slopes (c) Nyquist plot for $NiCl_2$dppp, GA, & NiGA (d) Molecular electrostatic potential map for $NiCl_2$dppp SMC (e) Band structure of GA, $NiCl_2$dppp and NiGA (f) Gibbs free energy of the adsorption of OER reaction intermediates over $NiCl_2$dppp, NiGA, RuO_2, and GA. (g) Total density of states (TDOS) profile of $NiCl_2$dppp, GA, and NiGA.

Magnetic field-assisted OER studies. Recent reports indicate that magnetic single atom catalysts can facilitate spin selective OER process.[92] Hence, for the first time, leveraging the in-situ changes in coordination and geometry of our complex, which created paramagnetic Ni centers (unpaired electrons), we investigate the possibility of using our NiGA catalyst (with the best OER activity) for spin-selective OER catalysis. Hence, we conducted OER LSV measurements in the presence and absence of a magnetic field (0.3 T) to investigate the effect of a magnetic field on the OER activity (the experimental procedure and setup is shown in supporting information). Applying an external magnetic field (perpendicular to the electrode orientation) resulted in superior OER performance in NiGA, potentially due to the induced spin selection. Figure 5a shows the OER LSV polarization curves for NiGA with (H_{on}, red line) and without (H_{off}, black line) an external magnetic field. The inset of figure 5a shows the schematic of the external magnetic field-aided OER studies. It is evident from the figure that under the magnetic field, the onset potential decreased from 1.49 V vs. RHE to 1.46 V vs. RHE (η_{10} changed from 400 mV to 340 mV) for NiGA. Further, the maximum current density increased from 11.2 mA cm^{-2} (H_{off}) to 32.5 mA cm^{-2} (H_{on}), leading to a magnetocurrent density of 21.3 mA^{-1} (shown in Figure S19), confirming the increased OER activity under magnetic field. The Tafel slope for NiGA under magnetic field decreased from 59.1 to 48.7 $mVdec^{-1}$, indicating that the RDS is still the second O* formation step (Figure S19). The Faradaic efficiency (FE) of

the OER also showed an improvement under magnetic field (from 96% without magnetic field to 97.5 % under magnetic field) (Figure S20). The corresponding OER polarization curve for $NiCl_2$dppp under the magnetic field is shown in Figure S21. A similar magnetic field-induced enhancement in the activity observed in the case of $NiCl_2$dppp indicates that the origin of magnetic field-enhanced activity observed in the NiGA SMC is from the complex. Interestingly, NiGA under magnetic field outperformed most of the state-of-the-art OER electrocatalysts, including RuO_2.[60]

To identify the spin selectivity effect behind the observed magnetic field-induced enhancement and eliminate any possible contribution from other indirect effects, including magnetohydrodynamic (MHD)[95] and magnetic hypothermia effects, we conducted a series of control measurements. Magnetic hypothermia is only relevant in an alternating magnetic field and is therefore not applicable in this study, where we use a permanent magnet. As the first control study, we measured the magnetocurrent density at different temperatures, as shown in Figure 5b and Figures S22i and S22ii. Although an initial increase in activity was observed, beyond 60°C, the magnetocurrent density decreased. Our microscopic and spectroscopic analysis confirmed that the NiGA and $NiCl_2$dppp samples underwent no structural or morphological degradation at 60°C (Figure S23, S24a, S24b, and S25). Hence, the observed decrease in activity could be attributed to the temperature-induced randomization of spins at the Ni center, which reduces the spin-selected activity of the catalyst under a magnetic field.[55] Another possible mechanism through which a magnetic field can enhance the catalytic process is via the MHD effect,[95] where the Lorentz force aided faster bubble removal from the electrode causes enhanced mass transfer and increases the catalytic activity. To investigate this, we performed LSV measurements using a rotating disk electrode (RDE), which constantly stirs the electrolyte during the experiments for NiGA (Figure 5c) and $NiCl_2$dppp (Figure S26). As expected, the agitation of the electrolyte slightly improved the activity compared to the stationary electrolyte. However, even under the agitation of the electrolyte, a significant increase in current density was observed upon applying a magnetic field, confirming that the enhancement garnered in the NiGA system under the magnetic field is primarily due to spin effects in the system. Kelvin force is another potential indirect effect that can act under a magnetic field to increase activity. However, Kelvin force is more pronounced under a non-uniform magnetic field. Since we are applying a static field using a permanent magnet over a small electrode area (0.07065 cm^2), we do not expect any non-uniformity of the field and hence exclude any contribution from the Kelvin force.[56] Another potential effect of a magnetic field is Maxwell stress, which arises from the interaction of the field with species having a dipole moment. To investigate this, we analyzed the electrochemical active surface area (ECSA) of NiGA with and without a magnetic field, as any Maxwell stress effect would be manifested by a change in ECSA (Figure S27). Our measurements showed no appreciable change in ECSA under a magnetic field, indicating no apparent Maxwell stress effect in our sample.[56] Hence, our control measurements have ruled out the possibility of any significant contribution from other indirect effects,

including MHD, Kelvin force, and Maxwell stress, and have confirmed that the observed enhancement is mostly due to spin effects in the system. Furthermore, we analyzed the stability of the NiGA complex and its activity under a magnetic field using chronoamperometry (100h). During our experiment (Figure S28), the sample retained >98% activity, demonstrating the stability of the catalysts. Our post-catalytic spectroscopic and microscopic evaluation of the NiGA catalyst (Figure S23, S24 and S25) also proved that the catalysts did not undergo any structural changes during the catalysis, again indicating the stability. Control experiments and stability analysis on $NiCl_2$dppp also yielded similar results, indicating an identical spin selective OER mechanism and stability in the complex as well.

Our spin density analysis demonstrated that, compared to the spin density in the absence of a magnetic field (random coupling), the spin alignment with spin polarized DFT leads to a higher spin density in NiGA around the Ni center. The calculation indicates that the spin density at the Ni center in $[NiCl_2(dppp)(OH)]^-$ is ~ 0.65 without spin alignment and ~ 0.82 with spin alignment (Figure 5d). As the spin density is directly proportional to the magnetic moment, the observation indicates a ferromagnetic ordering of electrons on the Ni center. This higher magnetic moment leads to heightened interaction between the magnetic Ni center and the adsorbed oxygen species and leads to a smaller electron–electron repulsion and a spin-dependent conductivity channel to enhance OER.[96] Thus, we propose a spin-dependent OER mechanism on Ni active sites on NiGA SMC (Figure 5e). As confirmed by our experiments (Figure 3), under alkaline conditions, the geometry and coordination environment of $NiCl_2$dppp undergoes a transition from a square planar to a TBP geometry, resulting in the Ni center possessing two unpaired electrons. When an external magnetic field is applied, it is favorable for the unpaired electron to be aligned in the direction of the magnetic field.[96] The electron transfer at the catalyst-adsorbate interface occurs via tunneling, with the highest tunneling probability achieved when electrons in both the catalyst and adsorbate possess identical spin alignment.[97] This phenomenon results in an energy splitting of the spin up (↑) and spin down (↓) levels at the magnetic center (Ni center here), thereby generating spin polarization and reducing the tunneling barrier for a particular spin, such as spin up (↑). The spin polarization selectively facilitates electron transfer (e.g., spin up (↑)) from the adsorbed OH^- ion to the NiGA SMC, as illustrated in the schematic (Figure 5f), with stabilization occurring through exchange interactions. This selective electron transfer process produces a spin-down $O(\downarrow)^-$ species, leading to the formation of a triplet-state intermediate, O(↓)O(↓)H, with a lower activation energy barrier. Ultimately, the triplet-state intermediate O(↓)O(↓)H species promotes the generation of triplet-state O_2, thereby enhancing OER activity, as reported previously in isolated metal sites.

To verify the proposed mechanism involving the in-situ generated paramagnetic Ni center under alkaline conditions, we carried out magnetic OER measurements under acidic conditions (Figure S29). The limited availability of OH^- anchoring in acidic conditions prevents geometry transitions for $NiCl_2$dppp in the acidic

medium. Since $NiCl_2$dppp is diamagnetic, no influence is expected in the acidic environment. As expected, our results did not show any improvement in OER activity, which confirmed that under acidic conditions, $NiCl_2$dppp does not undergo the required geometry transition and no unpaired electrons are present to facilitate spin polarization. To understand the energetic foundation behind the spin-dependent activity, we leveraged spin-dependent DFT analysis and investigated the effect of spin alignment on the free energy of adsorption at various OER steps. The energy diagram with and without spin alignment for NiGA at 0 V (vs RHE) to produce triplet oxygen is shown in Figure 5f. Our analysis indicates that all the oxo-adsorbed species involved in the OER reaction require lower energy under spin alignment, indicating that the process is more thermodynamically favorable. Thus, the lower free energy in the spin-aligned catalyst explains the observed enhancement of OER activity under magnetic field, in our study.

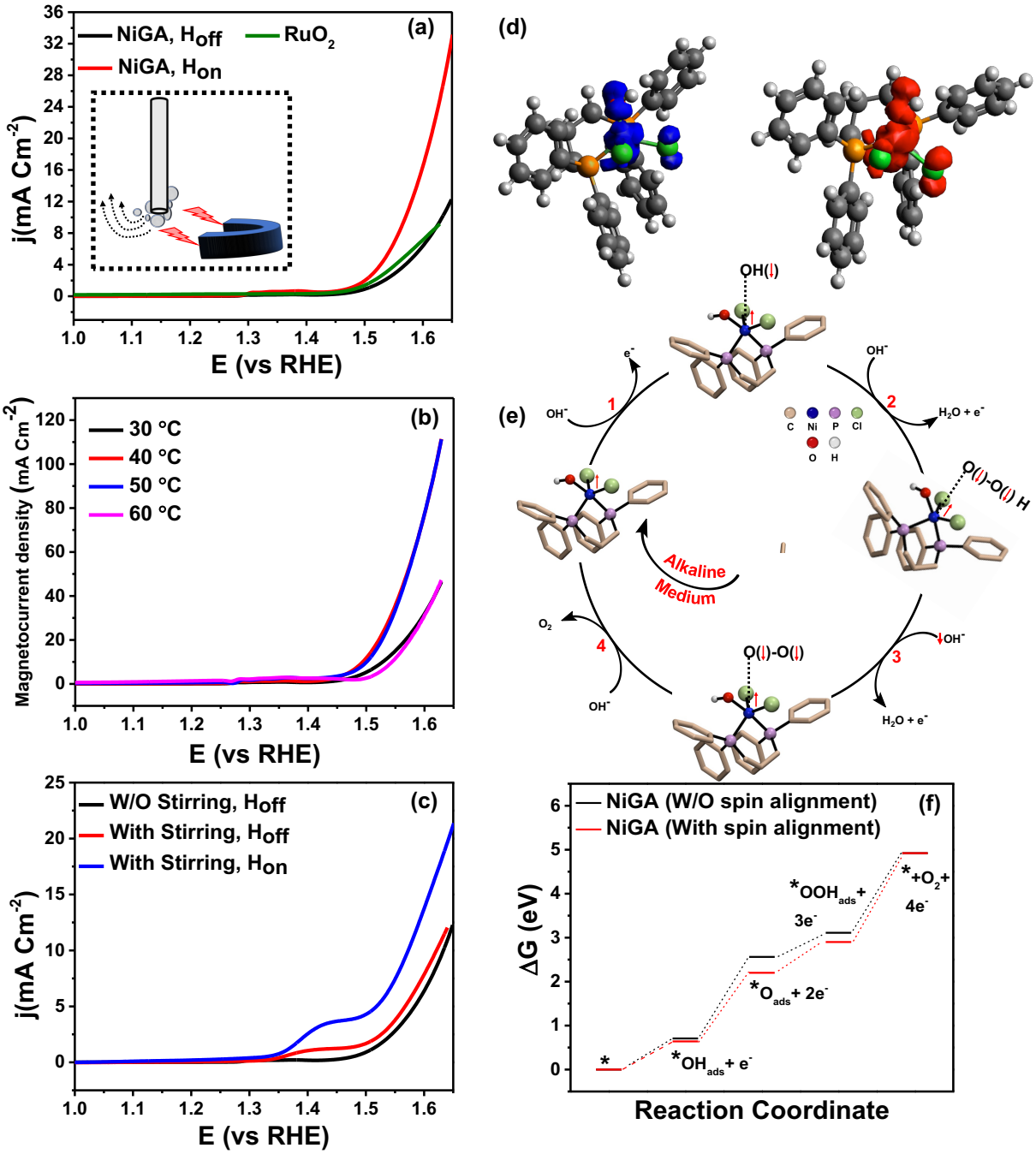

Figure 5 (a) Comparison of OER LSV curves under the magnetic field ~0.3T (H_{on} vs Ho_{ff}) for NiGA (b) Variation in magnetocurrent density for NiGA when temperature is increased from 30 ºC to 60 ºC (c) LSV curves measured in an RDE set up under stirring (1200 rpm) to verify the magnetohydrodynamic (MHD) effect (d) Spin density for $[NiCl_2(dppp)(OH)]^-$ without (blue region) and with (red- region) spin alignment (e) Proposed spin-selective OER mechanism (f) Gibbs free energy of the adsorption of OER reaction

intermediates over NiGA with and without spin alignment.

Conclusions

In this study, we identified an SMC consisting of a coordination complex, $NiCl_2$dppp, supported on GA, under the assistance of a magnetic field, that surpasses the OER activity of benchmark RuO_2 catalysts by facilitating spin-selective OER catalysis. By employing various spectroscopic and microscopic techniques, we characterized the prepared SMC and confirmed that the Ni centers in the $NiCl_2$dppp molecules are the active sites. Our analysis demonstrated that immobilizing $NiCl_2$dppp on GA results in an interfacial charge transfer from the Ni center to GA due to the favorable band alignment between $NiCl_2$dppp and GA in the SMC. This charge transfer further activates the Ni center for OER, enhancing its catalytic activity. Moreover, we established that, under highly alkaline conditions, the complex undergoes a geometrical transition, leading to the electronic redistribution of the Ni center, making it paramagnetic. Consequently, under a static magnetic field, the unpaired electron in the Ni center aligns parallel to the magnetic field, enabling low energy, spin-selective transfer of electrons with the same spin from the adsorbed oxygen species and enhancing OER catalytic activity. As a result, the OER overpotential (η_{10}) under the magnetic field decreased to 340 mV, while the maximum current density increased by ~ 300%. Through various control experiments, we demonstrated that the observed enhancement in OER activity is attributed to spin-selective electron transfer rather than any indirect magnetic field-induced effects. Our theoretical investigation supported the alignment of electrons at the Ni center, as evidenced by the increased spin density under the magnetic field, and showed that the reaction becomes energetically more favorable, leading to significantly improved OER kinetics. These findings indicate the need to study potential in-situ geometrical changes in active sites for inorganic molecules during OER and will inspire the development of novel SMCs as highly active OER catalysts.

Acknowledgements

The authors express gratitude to Dr. Mohamed F. Sanad for the discussions. S.T.S. acknowledges the financial support provided through UTEP startup and UT STARs, and the partial support from DOE under grant # DE-FE0031908. S.T.S also acknowledges the partial support through NSF-PREM grant #DMR-1827745. A portion of this research was performed at the Center for Integrated Nanotechnologies, which is an Office of Science User Facility operated for the U.S. Department of Energy (DOE) Office of Science by Los Alamos National Laboratory (Contract 89233218CNA000001) and Sandia National Laboratories (Contract DE-NA-0003525). Sandia National Laboratories is a multimission laboratory managed and operated by National Technology & Engineering Solutions of Sandia, LLC, a wholly owned subsidiary of Honeywell International, Inc., for the U.S. DOE's National Nuclear Security Administration. The views expressed in the article do not necessarily represent the views of the U.S. DOE or the United States

Government.The authors also acknowledge the utilization of facilities at the Eyring Materials Center at Arizona State University, supported in part of Nanotechnology collaborative Infrastructure (NCI)-Southwest by NSF program NNCI-ECCS-1542160. The authors also acknowledge the the Center for High-Energy X-ray Sciences (CHEXS), which is supported by the National Science Foundation (BIO, ENG and MPS Directorates) under award DMR-1829070.

References

[1] K. A. Stoerzinger, L. Qiao, M. D. Biegalski, Y. Shao-Horn, *J. Phys. Chem. Lett.* **2014**, *5*, 1636.

[2] W. T. Hong, M. Risch, K. A. Stoerzinger, A. Grimaud, J. Suntivich, Y. Shao-Horn, *Energy Environ. Sci.* **2015**, *8*, 1404.

[3] Y. Yan, B. Y. Xia, B. Zhao, X. Wang, *J. Mater. Chem. A* **2016**, *4*, 17587.

[4] D. Zhao, Z. Zhuang, X. Cao, C. Zhang, Q. Peng, C. Chen, Y. Li, *Chem. Soc. Rev.* **2020**, *49*, 2215.

[5] R. Gusmão, M. Veselý, Z. Sofer, *ACS Catal.* **2020**, *10*, 9634.

[6] D. Wang, Q. Li, C. Han, Q. Lu, Z. Xing, X. Yang, *Nat. Commun.* **2019**, *10*, 1.

[7] Y. Yao, S. Hu, W. Chen, Z. Q. Huang, W. Wei, T. Yao, R. Liu, K. Zang, X. Wang, G. Wu, W. Yuan, T. Yuan, B. Zhu, W. Liu, Z. Li, D. He, Z. Xue, Y. Wang, X. Zheng, J. Dong, C. R. Chang, Y. Chen, X. Hong, J. Luo, S. Wei, W. X. Li, P. Strasser, Y. Wu, Y. Li, *Nat. Catal.* **2019**, *2*, 304.

[8] J. Kibsgaard, I. Chorkendorff, *Nat. Energy* **2019**, *4*, 430.

[9] G. A. Lawrance, *Introduction to Coordination Chemistry*, Wiley, **2010**.

[10] J. L. Fillol, Z. Codolà, I. Garcia-Bosch, L. Gàmez, J. J. Pla, M. Costas, *Nat. Chem.* **2011**, *3*, 807.

[11] L. Ouahab, *Coord. Chem. Rev.* **1998**, *178–180*, 1501.

[12] B. J. Coe, N. R. M. Curati, *Comments Inorg. Chem.* **2004**, *25*, 147.

[13] Y. Zhao, Z. Song, X. Li, Q. Sun, N. Cheng, S. Lawes, X. Sun, *Energy Storage Mater.* **2016**, *2*, 35.

[14] Z. Hu, B. J. Deibert, J. Li, *Chem. Soc. Rev.* **2014**, *43*, 5815.

[15] J. Chen, Y. Zhang, H. Ye, J. Q. Xie, Y. Li, C. Yan, R. Sun, C. P. Wong, *ACS Appl. Energy Mater.* **2019**, *2*, 2734.

[16] W. L. Leong, J. J. Vittal, *Chem. Rev.* **2011**, *111*, 688.

[17] S. Elmas, T. J. Macdonald, W. Skinner, M. Andersson, T. Nann, *Polymers (Basel).* **2019**, *11*, 1.

[18] C. Xu, H. Wang, Q. Wang, Y. Wang, Y. Zhang, G. Fan, *Appl. Surf. Sci.* **2019**, *466*, 193.

[19] B. Zhou, J. J. Zheng, J. Duan, C. Hou, Y. Wang, W. Jin, Q. Xu, *ACS Appl. Mater. Interfaces* **2019**, *11*, 21086.

[20] K. C. Gupta, A. K. Sutar, *Coord. Chem. Rev.* **2008**, *252*, 1420.

[21] M. Tsutsui, A. Courtney, in *Mol. Rearrange.* (Eds.: F. G. A. Stone, R. B. T.-A. in O. C. West), Academic Press, **1977**, pp. 241–282.

[22] J. Masud, P. C. Ioannou, N. Levesanos, P. Kyritsis, M. Nath, *ChemSusChem* **2016**, *9*, 3128.

[23] A. Macchioni, *Front. Catal.* **2021**, *1*, 1.

[24] V. Cadierno, *Catalysts* **2021**, *11*, 11.

[25] J. Li, R. Güttinger, R. Moré, F. Song, W. Wan, G. R. Patzke, *Chem. Soc. Rev.* **2017**, *46*, 6124.

[26] M. A. Asraf, H. A. Younus, M. Yusubov, F. Verpoort, *Catal. Sci. Technol.* **2015**, *5*, 4901.

[27] *Supported Metal Complexes: A New Generation of Catalysts*, Springer Science & Business Media, **1985**.

[28] C. K. Jørgensen, *J. Franklin Inst.* **1966**, *282*, 262.

[29] A. Heuer-Jungemann, N. Feliu, I. Bakaimi, M. Hamaly, A. Alkilany, I. Chakraborty, A. Masood, M. F. Casula, A. Kostopoulou, E. Oh, K. Susumu, M. H. Stewart, I. L. Medintz, E. Stratakis, W. J. Parak, A. G. Kanaras, *Chem. Rev.* **2019**, *119*, 4819.

[30] W. Zhou, Y. P. Wu, X. Wang, J. W. Tian, D. D. Huang, J. Zhao, Y. Q. Lan, D. S. Li, *CrystEngComm* **2018**, *20*, 4804.

[31] C. A. Downes, A. J. Clough, K. Chen, J. W. Yoo, S. C. Marinescu, *ACS Appl. Mater. Interfaces* **2018**, *10*, 1719.

[32] R. Dong, Z. Zheng, D. C. Tranca, J. Zhang, N. Chandrasekhar, S. Liu, X. Zhuang, G. Seifert, X. Feng, *Chem. - A Eur. J.* **2017**, *23*, 2255.

[33] S. C. Eady, M. M. MacInnes, N. Lehnert, *Inorg. Chem.* **2017**, *56*, 11654.

[34] S. Deng, E. Gao, Y. Wang, S. Sen, S. T. Sreenivasan, S. Behura, P. Král, Z. Xu, V. Berry, *ACS Nano* **2016**, *10*, 8403.

[35] J. Wang, X. Huang, S. Xi, J. M. Lee, C. Wang, Y. Du, X. Wang, *Angew. Chemie - Int. Ed.* **2019**, *58*, 13532.

[36] M. Gong, Y. Li, H. Wang, Y. Liang, J. Z. Wu, J. Zhou, J. Wang, T. Regier, F. Wei, H. Dai, *J. Am. Chem. Soc.* **2013**, *135*, 8452.

[37] R. D. L. Smith, M. S. Prévot, R. D. Fagan, S. Trudel, C. P. Berlinguette, *J. Am. Chem. Soc.* **2013**, *135*, 11580.

[38] Y. Qiu, L. Xin, W. Li, *Langmuir* **2014**, *30*, 7893.

[39] M. Gao, W. Sheng, Z. Zhuang, Q. Fang, S. Gu, J. Jiang, Y. Yan, *J. Am. Chem. Soc.* **2014**, *136*, 7077.

[40] M. W. Louie, A. T. Bell, *J. Am. Chem. Soc.* **2013**, *135*, 12329.

[41] M. Zhang, M.-T. Zhang, C. Hou, Z.-F. Ke, T.-B. Lu, *Angew. Chemie* **2014**, *126*, 13258.

[42] Y. Han, Y. Wu, W. Lai, R. Cao, *Inorg. Chem.* **2015**, *54*, 5604.

[43] G. Y. Luo, H. H. Huang, J. W. Wang, T. B. Lu, *ChemSusChem* **2016**, *9*, 485.

[44] D. R. Kauffman, D. Alfonso, D. N. Tafen, J. Lekse, C. Wang, X. Deng, J. Lee, H. Jang, J. S. Lee, S. Kumar, C. Matranga, *ACS Catal.* **2016**, *6*, 1225.

[45] G. W. Sievers, A. W. Jensen, J. Quinson, A. Zana, F. Bizzotto, M. Oezaslan, A. Dworzak, J. J. K. Kirkensgaard, T. E. L. Smitshuysen, S. Kadkhodazadeh, M. Juelsholt, K. M. Ø. Jensen, K. Anklam, H. Wan, J. Schäfer, K. Čépe, M. Escudero-Escribano, J. Rossmeisl, A. Quade, V. Brüser, M. Arenz, *Nat. Mater.* **2021**, *20*, 208.

[46] L. Bu, N. Zhang, S. Guo, X. Zhang, J. Li, J. Yao, T. Wu, G. Lu, J. Y. Ma, D. Su, X. Huang, *Science (80-.).* **2016**, *354*, 1410.

[47] H. Sun, Z. Yan, F. Liu, W. Xu, F. Cheng, J. Chen, *Adv. Mater.* **2020**, *32*, 1.

[48] Y. Pan, R. Abazari, Y. Wu, J. Gao, Q. Zhang, *Electrochem. commun.* **2021**, *126*, 107024.

[49] G. Chen, W. Zhou, D. Guan, J. Sunarso, Y. Zhu, X. Hu, *Sci. Adv.* **2017**, 1.

[50] H. Mistry, A. S. Varela, S. Kühl, P. Strasser, B. R. Cuenya, *Nat. Rev. Mater.* **2016**, *1*, DOI 10.1038/natrevmats.2016.9.

[51] J. K. Nørskov, T. Bligaard, J. Rossmeisl, C. H. Christensen, *Nat. Chem.* **2009**, *1*, 37.

[52] I. C. Man, H. Y. Su, F. Calle-Vallejo, H. A. Hansen, J. I. Martínez, N. G. Inoglu, J. Kitchin, T. F. Jaramillo, J. K. Nørskov, J. Rossmeisl, *ChemCatChem* **2011**, *3*, 1159.

[53] J. Gracia, *Phys. Chem. Chem. Phys.* **2017**, *19*, 20451.

[54] J. Gracia, R. Sharpe, J. Munarriz, *J. Catal.* **2018**, *361*, 331.

[55] F. A. Garcés-Pineda, M. Blasco-Ahicart, D. Nieto-Castro, N. López, J. R. Galán-Mascarós, *Nat. Energy* **2019**, *4*, 519.

[56] Y. Zhang, C. Liang, J. Wu, H. Liu, B. Zhang, Z. Jiang, S. Li, P. Xu, *ACS Appl. Energy Mater.* **2020**, *3*, 10303.

[57] S. Jiang, F. Chen, L. Zhu, Z. Yang, Y. Lin, Q. Xu, Y. Wang, *ACS Appl. Mater. Interfaces* **2022**, *14*, 10227.

[58] T. Z. Fahidy, *J. Appl. Electrochem.* **2002**, *32*, 551.

[59] J. Ge, R. R. Chen, X. Ren, J. Liu, S. J. H. Ong, Z. J. Xu, *Adv. Mater.* **2021**, *33*, 1.

[60] T. Wu, X. Ren, Y. Sun, S. Sun, G. Xian, G. G. Scherer, A. C. Fisher, D. Mandler, J. W. Ager, A. Grimaud, J. Wang, C. Shen, H. Yang, J. Gracia, H. J. Gao, Z. J. Xu, *Nat. Commun.* **2021**, *12*, 1.

[61] Z. Li, Z. Wang, S. Xi, X. Zhao, T. Sun, J. Li, W. Yu, H. Xu, T. S. Herng, X. Hai, P. Lyu, M. Zhao, S. J. Pennycook, J. Ding, H. Xiao, J. Lu, *ACS Nano* **2021**, *15*, 7105.

[62] G. Zhou, P. Wang, H. Li, B. Hu, Y. Sun, R. Huang, L. Liu, *Nat. Commun.* **2021**, *12*, 1.

[63] R. Shukla, D. Chopra, *Curr. Sci.* **2021**, *120*, 1848.

[64] B. You, N. Jiang, M. Sheng, M. W. Bhushan, Y. Sun, *ACS Catal.* **2016**, *6*, 714.

[65] A. Yadav, P. Kelich, N. Kallmyer, N. F. Reuel, L. Vuković, *ACS Appl. Mater. Interfaces* **2023**, *15*, 24084.

[66] P. Nguyen, J. Li, T. S. Sreeprasad, K. Jasuja, N. Mohanty, M. Ikenberry, K. Hohn, V. B. Shenoy, V. Berry, *Small* **2013**, *9*, 3823.

[67] Y. Li, Z. S. Wu, P. Lu, X. Wang, W. Liu, Z. Liu, J. Ma, W. Ren, Z. Jiang, X. Bao, *Adv. Sci.* **2020**, *7*, DOI 10.1002/advs.201903089.

[68] X. Cao, G. Tian, Y. Chen, J. Zhou, W. Zhou, C. Tian, H. Fu, *J. Mater. Chem. A* **2014**, *2*, 4366.

[69] M. F. Sanad, V. S. N. Chava, A. E. Shalan, L. G. Enriquez, T. Zheng, S. Pilla, S. T. Sreenivasan, *ACS Appl. Mater. Interfaces* **2021**, *13*, 40731.

[70] H. J. Choi, M. P. Suh, *J. Am. Chem. Soc.* **1998**, *120*, 10622.

[71] C. M. Donahue, S. P. McCollom, C. M. Forrest, A. V. Blake, B. J. Bellott, J. M. Keith, S. R. Daly, *Inorg. Chem.* **2015**, *54*, 5646.

[72] D. Sasi, V. Ramkumar, N. N. Murthy, *ACS Omega* **2017**, *2*, 2474.

[73] C. W. MacHan, A. M. Spokoyny, M. R. Jones, A. A. Sarjeant, C. L. Stern, C. A. Mirkin, *J. Am. Chem. Soc.* **2011**, *133*, 3023.

[74] E. S. Wiedner, A. M. Appel, S. Raugei, W. J. Shaw, R. Morris Bullock, *Chem. Rev.* **2022**, *122*, 12427.

[75] M. Ferbinteanu, A. F. Cimpoesu, A. Mariusandruh, F. D. Rochon, *Polyhedron* **1998**, *17*, 3671.

[76] A. G. Blackman, E. B. Schenk, R. E. Jelley, E. H. Krenske, L. R. Gahan, *Dalt. Trans.* **2020**, *49*, 14798.

[77] K. E. R. Marriott, L. Bhaskaran, C. Wilson, M. Medarde, S. T. Ochsenbein, S. Hill, M. Murrie, *Chem. Sci.* **2015**, *6*, 6823.

[78] H. Olivier-Bourbigou, P. A. R. Breuil, L. Magna, T. Michel, M. F. Espada Pastor, D. Delcroix, *Chem. Rev.* **2020**, *120*, 7919.

[79] G. R. Van Hecke, W. D. Horrocks, *Inorg. Chem.* **1966**, *5*, 1968.

[80] S. M. Abozeid, E. M. Snyder, A. P. Lopez, C. M. Steuerwald, E. Sylvester, K. M. Ibrahim, R. R. Zaky, H. M. Abou-El-Nadar, J. R. Morrow, *Eur. J. Inorg. Chem.* **2018**, *2018*, 1902.

[81] S. Neukermans, M. Samanipour, H. Y. Vincent Ching, J. Hereijgers, S. Van Doorslaer, A. Hubin, T. Breugelmans, *ChemElectroChem* **2020**, *7*, 4578.

[82] J. Krzystek, J. H. Park, M. W. Meisel, M. A. Hitchma, H. Stratemeier, L. C. Brunel, J. Telser, *Inorg. Chem.* **2002**, *41*, 4478.

[83] H. Chen, D. Ge, J. Chen, R. Li, X. Zhang, T. Yu, Y. Wang, S. Song, *Chem. Commun.* **2020**, *56*, 10529.

[84] M. K. Wojnar, D. W. Laorenza, R. D. Schaller, D. E. Freedman, *J. Am. Chem. Soc.* **2020**, *142*, 14826.

[85] J. Löliger, R. Scheffold, *J. Chem. Educ.* **1972**, *49*, 646.

[86] M. J. Baldwin, T. L. Stemmler, P. J. Riggs-Gelasco, E. P. H. James, V. L. Pecoraro, M. L. Kirk, *J. Am. Chem. Soc.* **1994**, *116*, 11349.

[87] M. M. Najafpour, H. Feizi, *Dalt. Trans.* **2018**, *47*, 6519.

[88] C. Hu, Q. Q. Huang, H. B. Xu, Y. Zhang, X. Peng, M. H. Zeng, *Inorg. Chem. Front.* **2021**, *8*, 2486.

[89] J. Abbenseth, J. M. Goicoechea, *Chem. Sci.* **2020**, *11*, 9728.

[90] A. R. Puente Santiago, T. He, O. Eraso, M. A. Ahsan, A. N. Nair, V. S. N. Chava, T. Zheng, S. Pilla, O. Fernandez-Delgado, A. Du, S. T. Sreenivasan, L. Echegoyen, *J. Am. Chem. Soc.* **2020**, *142*, 17923.

[91] A. N. Nair, M. F. Sanad, V. S. N. Chava, S. T. Sreenivasan, *Chem. Commun.* **2022**, *58*, 10368.

[92] Z. Sun, L. Lin, J. He, D. Ding, T. Wang, J. Li, M. Li, Y. Liu, Y. Li, M. Yuan, B. Huang, H. Li, G. Sun, *J. Am. Chem. Soc.* **2022**, DOI 10.1021/jacs.2c01153.

[93] Y. Lee, J. Suntivich, K. J. May, E. E. Perry, Y. Shao-Horn, *J. Phys. Chem. Lett.* **2012**, *3*, 399.

[94] L. Trotochaud, J. K. Ranney, K. N. Williams, S. W. Boettcher, *J. Am. Chem. Soc.* **2012**, *134*, 17253.

[95] B. Seo, S. H. Joo, *Nat. Energy* **2018**, *3*, 451.

[96] C. Biz, M. Fianchini, J. Gracia, *ACS Catal.* **2021**, *11*, 14249.

[97] J. Li, J. Ma, Z. Ma, E. Zhao, K. Du, J. Guo, T. Ling, *Adv. Energy Sustain. Res.* **2021**, *2*, 2100034.